

3D Heterogeneous Integration of Silicon Nitride and Aluminum Nitride on Sapphire toward Ultra-wideband Photonics Integrated Circuits

Liang Zhang,^{*,†,‡} Yanan Guo,^{*,†,‡} Junxi Wang,^{†,‡} Jinmin Li,[†] and Jianchang
Yan^{*,†,‡}

[†]*Research and Development Center for Wide Bandgap Semiconductors, Institute of
Semiconductors, Chinese Academy of Sciences, Beijing 100083, China*

[‡]*College of Materials Science and Opto-Electronic Technology, University of Chinese
Academy of Sciences, Beijing 100049, China*

E-mail: zhangliang@semi.ac.cn; ynguo@semi.ac.cn; yanjc@semi.ac.cn

Abstract

Extending two-dimensional photonic integrated circuits (PICs) to three-dimensional (3D) configurations promises great potential for scaling up integration, enhancing functionality, and improving performance of PICs. Silicon-based 3D PICs have made substantial progress due to CMOS compatibility. However, the narrow bandgap of silicon (1.1 eV) limits their use in short-wavelength applications, such as chemical and biological sensing, underwater optical communications, and optical atomic clocks. In this work, we developed a 3D photonics platform by heterogeneously integrating silicon nitride (SiN) and aluminum nitride (AlN) PICs on sapphire (Al_2O_3). The broadband transparency of these materials allow our platform to operate over a multi-octave wavelength ranging from ultraviolet to infrared. Leveraging this platform, we demonstrated efficient optical nonlinearity in an AlN microcavity, low-loss and tunable SiN

waveguide-based optical components, and optical linking between AlN and SiN PICs layers in the visible and near-infrared spectrum, hinting at potential applications in integrated quantum systems. Our work presents an ultra-wideband 3D PICs platform, providing new opportunities for broadband and short-wavelength applications of PICs.

Introduction

Photonics integrated circuits (PICs) have been widely developed and deployed, offering integrated solutions for various applications including telecommunications, computation, detection, and sensors.¹⁻⁵ Ever-increasing demands for data processing capabilities drive the need for large-scale PICs with more complex and numerous components.⁶⁻⁹ For traditional two-dimensional (2D) planar PICs, integrating a large number of photonic devices on a limited chip area generally necessitates many optical waveguide crossings.⁶⁻⁸ This, in turn, results in serious in-plane crossing loss,¹⁰ limiting the scalability of PICs. Inspired by 3D electronic integrated circuits (ICs) that leverage multiple metal interconnect levels for on-chip connectivity,^{11,12} extending 2D PICs to 3D structures through vertical stacking and coupling, provides a feasible solution for compact and highly dense large-scale PICs.¹³⁻¹⁵

Harnessing established CMOS manufacturing, silicon-based 3D PICs have achieved significant advancements, enabling demonstrations such as large-scale optical phased arrays,¹⁶ efficient optical transceivers,¹⁷ high-density optical switches,¹⁸ and integrated on-chip lasers,¹⁹ etc. However, silicon's inherently narrow bandgap restricts its applications beyond telecommunications band, especially in fields that require shorter wavelengths, such as atomic physics, augmented and virtual reality, and bio-sensing.²⁰ Heterogeneous integration with wideband materials is a straightforward way to bypass this limitation.²¹ So far, 3D PICs on silicon substrates in ultraviolet and visible bands have been developed through vertical integration with silicon nitride (SiN),^{22,23} aluminum oxide (Al₂O₃),²⁴⁻²⁶ and sputtered aluminum nitride (AlN).^{27,28} These have been implemented for ion trapping,²⁹ light detection,³⁰ piezo-actuated modulators,³¹ etc.

Compared to popular integrated materials such as silicon (Si), gallium arsenide/indium phosphide (GaAs/InP) and lithium niobate (LiNbO₃), SiN, Al₂O₃ and AlN have much broader optical windows spanning from ultraviolet to infrared wavelengths. Notably, they are transparent in the ultraviolet spectrum (wavelengths below 400 nm), a region inaccessible to most widely used integrated materials. This property is highly valued for current short-wavelength integrated photonics.³² Furthermore, they exhibit low optical propagation losses, comparable to those of other materials within corresponding spectral bands. For clarity, we summarized the reported optical propagation losses in waveguides of these materials in their transparent spectral windows in Figure 1a.^{24,29,33–41,41–65} The optical losses tend to increase at higher frequencies due to stronger scattering caused by waveguide surface roughness and intrinsic material absorption. Technological advancements in material preparation and nanofabrication processes hold promise for substantially minimizing these losses, potentially approaching the low loss levels observed in the infrared band. Due to broadband and low-loss characteristics, SiN, AlN, and Al₂O₃ are excellent candidates for ultra-wideband 3D heterogeneous PIC systems.

In this work, we developed a 3D PIC platform by vertically integrating SiN and AlN PICs on sapphire substrate, offering ultra-broad optical transparency from ultraviolet to infrared spectrum. To evaluate the platform’s robustness, we demonstrated both nonlinear and linear optical processes in visible (VI) and near-infrared (IR) spectral regions with fundamental components of the platform. A low-loss AlN microring, vertically coupled with a SiN waveguide, was fabricated, achieving intrinsic quality factors of 2.36×10^6 and 3.35×10^5 for near-IR and VI wavelength bands, respectively. This enabled efficient second harmonic generation (SHG) with an efficiency of 12598 %/W and spontaneous parametric down-conversion (SPDC) with a single-photon generating rate of 24 MHz/mW. We also built essential SiN optical components of the platform, operating in both IR and VI ranges, including high-Q microcavities, low-loss waveguide spirals, wavelength division multiplexers, and tunable Mach-Zehnder interferometers. Additionally, vertical coupling between AlN and SiN

PICs was also demonstrated. Our work presents a 3D SiN-AlN PICs with high-performance linearity and nonlinearity, showing great potential for integrated quantum photonics.

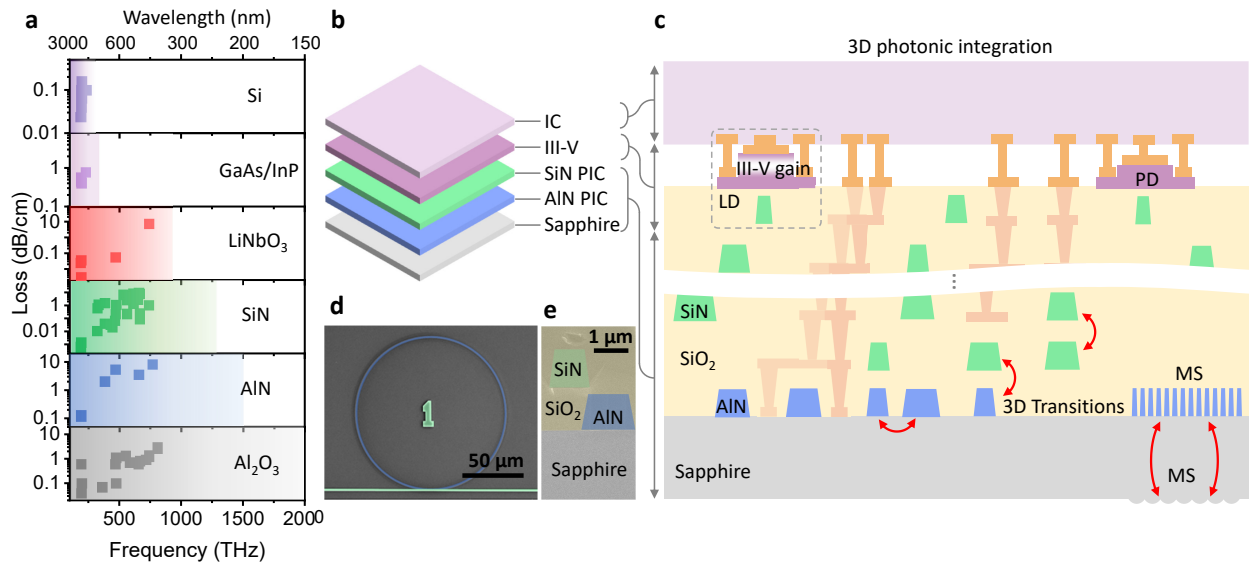


Figure 1: **3D heterogeneous PICs.** **a**, Comparison of optical loss and transparent window (color-shading area) between popular integrated platforms and the materials used in this work. **b**, Concept of 3D heterogeneous PICs. **c**, Cross-section of this 3D PICs in **b**. That is envisioned future works with extended functionality, such as control ICs, III-V laser diodes (LDs) and photon detectors (PDs), scale-up multilayer heterogeneous SiN-AlN PICs and other optical microstructures. **d**, False-coloured scanning electron microscope (SEM) image of vertical integrated AlN microring and SiN waveguide. **e**, False-coloured SEM image of cross-section for stacked photonics waveguides on sapphire substrate.

Results

Ultra-wideband 3D PICs

The envisioned 3D PICs feature a layered architecture as shown in Figure 1b, consisting of ICs, a III-V gain layer, SiN and AlN PIC layers, and a sapphire substrate with integrated microstructures (MS). A typical cross-section is illustrated in Figure 1c. ICs serve as driving and control units, connected to PICs via wafer bonding.^{11,17,66} III-V materials provide active optical components like laser gain media and photodetectors.^{67,68} SiN waveguides have low optical losses spanning a broad spectrum from infrared to ultraviolet. Meanwhile, their ver-

tical stacking is highly compatible with standard CMOS fabrication processes, positioning them as an ideal platform for photon routing in 3D PICs. However, the centrosymmetric structure of SiN, inherently limits the critical functionalities of 3D PICs, such as efficient second-order optical nonlinearity and high-speed electro-optic modulation. AlN, featuring a high index (2.2) and large bandgap (6.2 eV), supports tightly confined, low-loss waveguides over ultra-wide band.⁶⁹ Moreover, AlN possesses strong $\chi^{(2)}$ nonlinearity, electro-optical effect, and intrinsic piezoelectricity, enabling essential photonic operations within the 3D PICs, including wavelength conversion via $\chi^{(2)}$ non-linearity and high-speed optical modulations.⁶⁹ The sapphire substrate, with a large bandgap (7.6 eV), provides an ultra-wide transparent window and is widely used in optical microstructures.⁷⁰ Interlayer optical transitions can be achieved via evanescent coupling between adjacent layers or through microstructures. Optical modulation and control circuits are linked through interlayer metals, similar to interconnections in ICs.

Foundation of our ultra-wideband 3D PIC concept is the heterogeneous integration of SiN and AlN. This approach exploits the fabrication compatibility of SiN and nonlinearity of AlN, thereby supporting the development of high-density, large-scale 3D PICs with advanced photonic functionalities. In this research, we focus on the integration of AlN and SiN PICs on sapphire substrate, using SiO₂ as cladding layer. The detailed fabrication process was described in the following section. A typical 3D PIC structure as shown in Figure 1d (captured during fabrication process), illustrates an AlN micro-ring (blue) on sapphire, surrounded by SiO₂, with a SiN bus waveguide (green) positioned above it. The cross-section of vertically integrated SiN and AlN waveguides is depicted in Figure 1e.

Fabrication of 3D PICs

The 3D PICs were fabricated following the process flow outlined in Figure 2a. Initially, the AlN waveguide structures were patterned using electron beam lithography (EBL) with Fox-16 resist. Following development in the TMAH developer, ICP dry etching with Cl₂/BCl₃/Ar

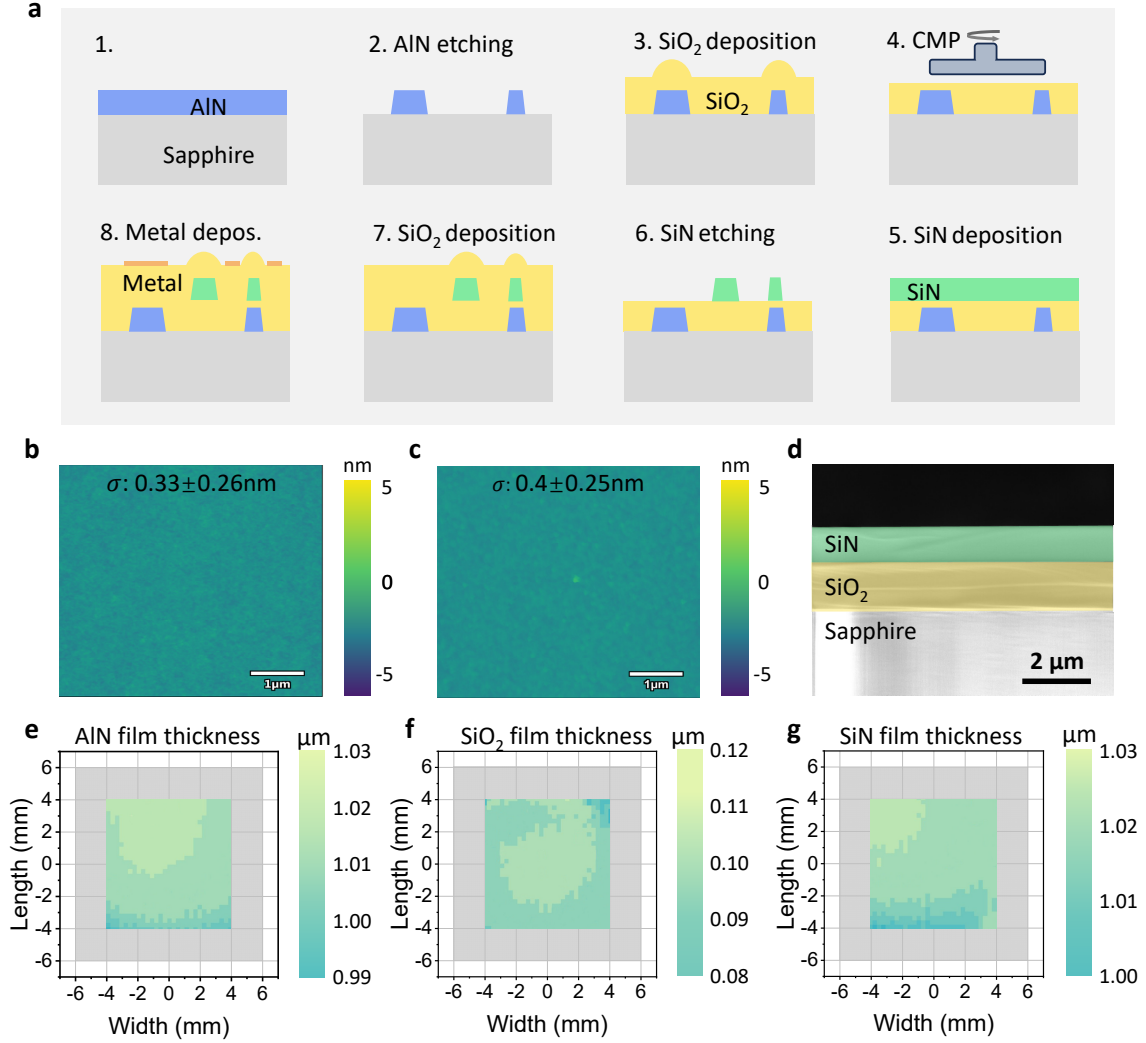


Figure 2: **Fabrication of 3D PICs.** **a**, Fabrication process flow of vertical heterogeneous integration of AlN and SiN PICs. **b**, Two dimensional (2D) atomic force microscopy (AFM) picture of polished SiO₂ surface with the root-mean-squared roughness (σ) of 0.33 ± 0.26 nm. **c**, 2D AFM picture of SiN surface with a σ of 0.4 ± 0.25 nm. **d**, False-coloured scanning electron microscope (SEM) image of cross-section of integrated multilayer on sapphire. Thickness mapping of AlN thin film (**e**), SiO₂ thin film deducting AlN thickness (**f**), and SiN thin film (**g**).

gases was used to etch AlN, transferring the patterns into the AlN layer. And then, a 1.5- μm -thick SiO₂ was deposited by PECVD to cover AlN waveguides. A 3-hour annealing at 1000°C in nitrogen atmosphere was performed to minimize the optical absorption of SiO₂ cladding layer. The SiO₂ surface was planarized by chemical mechanical polishing (CMP) using Fujimi PL-4217 Slurry and IC-1000 Polish pad. The polished SiO₂ surface has a roughness (σ) of 0.33 ± 0.26 nm (Figure 2b). Subsequently, a 1- μm -thickness SiN layer was deposited on the flattened SiO₂ by LPCVD (Figure 2d), yielding a surface roughness σ of 0.4 ± 0.25 nm (Figure 2c). We used MaN2410 resist to define SiN PICs patterns by EBL. After developing in MIF319 developer, HCF₃/O₂ chemistry was used to etch SiN. Afterwards, SiN PICs were annealed at 1000°C in nitrogen to reduce the optical absorption of SiN waveguides. Another 1.5- μm -thickness SiO₂ cladding layer was deposited and annealed following previous processes. Finally, Ti/Au metal stacked layers were deposited as the phase shifter to control the SiN and AlN PICs. We monitored the thickness of AlN, SiO₂ and SiN films during fabrication process. As depicted in Figure 2e, f and g, these films exhibited thickness variations within approximately ± 10 nm, indicating a commendable level of uniformity.

Optical non-linearity of AlN PICs

On-chip optical nonlinearity plays a crucial role in both classical and quantum photonics information processing. Single-crystalline AlN stands out as a prominent material for non-linear phenomena across telecom IR, visible, and ultraviolet wavelengths.^{58,71-74} To exhibit the nonlinearity of our 3D PICs, we fabricated an AlN micro-ring cavity and demonstrated efficient SHG and SPDC in visible and near-infrared spectra. As shown in Figure 3a, the micro-ring device comprises a 60- μm -radius (R_r) AlN ring on sapphire with a pulley SiN waveguide thereon. Both AlN ring and SiN layers are about 1 μm thick, separated by a 100-nm gap and encased in a thick SiO₂ cladding layer (inset of Figure 3a). Coupling between ring and waveguide was optimized using finite element simulations (Supplementary Section

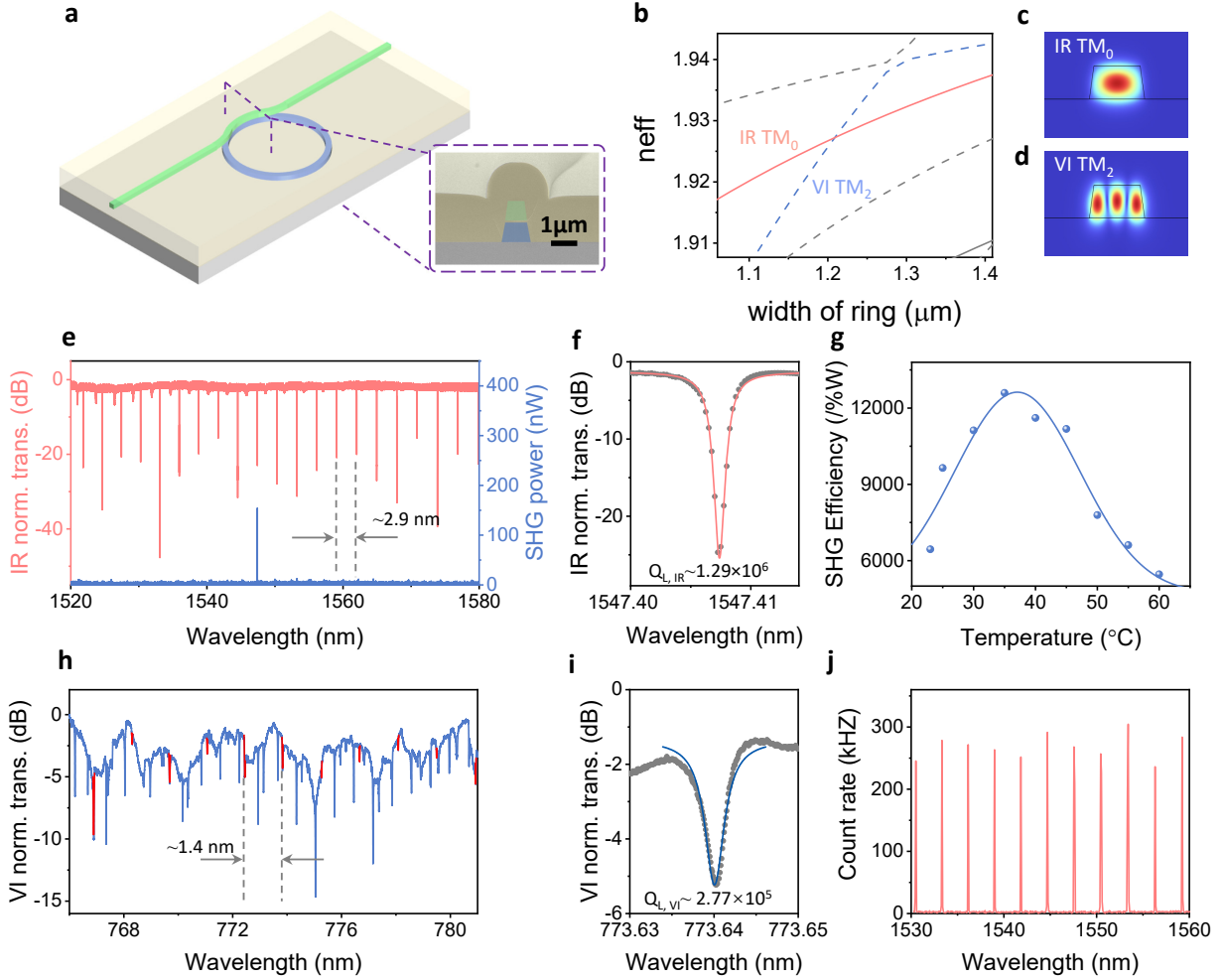


Figure 3: **SHG and SPDC of AlN PICs.** **a**, Heterogeneously integrated AlN micro-ring with a pully SiN waveguide. Inset shows a false-colored SEM image of cross-section of coupling area. **b**, Simulated optical effective refractive index (n_{eff}) of AlN ring waveguide for infrared (IR, red) and visible (VI, blue) modes. **c** and **d**, Optical IR TM_0 and VI TM_2 in AlN ring waveguide. **e**, IR transmission spectrum (red) and generated second harmonic generation (SHG) spectrum (blue) of AlN ring. **f**, Zoom-in view of the IR resonance in **e**, aligned with the SHG peak. The loaded quality factors ($Q_{L,IR}$) of this resonance is estimated to be about 1.29×10^6 by Lorentzian fitting. **g**, SHG efficiency tuned by temperature. **h**, VI transmission spectrum of AlN ring. TM_2 mode resonances are highlighted by red color. **i**, Zoom-in view of VI resonance in **h** aligned with the SHG peak. Its loaded quality ($Q_{L,VI}$) is about 2.77×10^5 . **j**, Single-photon spectrum generated via SPDC of AlN ring.

I).

Efficient SHG and SPDC require phase-matching that can be fulfilled by the fundamental transverse-magnetic IR mode (TM_0) and higher-order VI mode (TM_2) (Figure 3c and d). Their angular frequencies ($\omega_{vi,ir}$) and momentum ($m_{vi,ir}$) relate as $\omega_{vi} = \omega_{ir,1} + \omega_{ir,2}$ and $m_{vi} = m_{ir,1} + m_{ir,2}$, respectively, which require effective refractive indices matching for two modes, $n_{eff} = m_{vi,ir}c/\omega_{vi,ir}R_r$ (where c is the vacuum light speed). Numerical simulations of mode dispersion in AlN ring waveguides were performed to obtain n_{eff} . By engineering AlN microring waveguide width, 1550-nm TM_0 and 775-nm TM_2 reach effective refractive-index matching at a width of $\sim 1.2 \mu\text{m}$ (Figure 3b).

Linear optical properties of AlN microring were first characterized via transmission spectra (Supplementary Section IV). The IR spectrum (red) shows a free spectral range (FSR) of 2.9 nm for TM_0 mode (Figure 3e). A phase-matched IR resonance at 1547.66 nm aligns with SHG peak in VI spectrum (blue), indicating near-critical coupling. Its zoomed-in view is further presented in Figure 3f. Its loaded quality factor ($Q_{L,IR}$) and intrinsic quality factor ($Q_{in,IR}$) are 1.29×10^6 and 2.36×10^6 , respectively, corresponding to an IR optical propagation loss of 0.165 dB/cm. Figure 3h shows the visible transmission spectrum of AlN microring, featuring multiple mode families with FSRs around 1.45 nm. These resonances mainly include TM_0 , TE_0 and TM_2 modes, where TM_2 mode resonances are highlighted in red. The TM_2 mode aligning SHG peak of 773.82 nm is displayed in Figure 3i, indicating the loaded quality factor ($Q_{L,VI}$) of 2.77×10^5 and intrinsic quality ($Q_{in,VI}$) of 3.35×10^5 , corresponding to a VI optical propagation loss of 1.2 dB/cm.

As shown in Figure 3a, a 200-nW SHG power was observed with a 0.63-mW input pump power at wavelength of 1547.41 nm. Considering 20 % and 10 % edge coupling efficiencies of SiN waveguides for IR and VI modes, respectively, the on-chip SHG efficiency is estimated to be about 6450 %/W. To maximize this efficiency, we precisely aligned IR and VI resonances via thermal-optical effect for perfect phase matching (Supplementary section IV). At 38 °C, the SHG efficiency reached maximum value of 12598 %/W (Figure 3g), roughly consistent

with the theoretical value of 14878 %/W (Supplementary Section II).

Efficient SHG confirms phase-matching of optical modes in AlN microring and also indicates its potential for efficient SPDC. Next, we further demonstrated the single-photon generation by SPDC (Supplementary section IV). A 5-mW pump power launched at the visible TM_2 mode resonance at ~ 773.8 nm. Generated single photons were detected by a superconducting single-photon detector (SSPD). Figure 3j is the measured single photon spectrum with 13 peaks, which align with 13 IR resonances of AlN microrings, spanning a bandwidth over 30 nm. Considering pump/single photon input/output coupling efficiencies and photon loss (~ 6 dB) of measurement system, the single photon generation efficiency is about 24 MHz/mW, closely matching theoretical result of 26 MHz/mW (Supplementary section III).

Optical components of SiN PICs

In our 3D PICs, SiN waveguides hold a key position for photon guidance and manipulation, which typically require low optical propagation loss for SiN waveguide-based optical components. To assess these losses, we fabricated SiN spiral waveguides ($1\ \mu\text{m} \times 1.2\ \mu\text{m}$ cross-section) on $\text{SiO}_2/\text{sapphire}$, as shown in Figure 4a. Transmission intensities of TM_0 modes of waveguides with different lengths are plotted as dots in Figure 4b. By linearly fitting these data points, we extracted propagation losses of 0.14 dB/cm and 0.4 dB/cm for IR and VI wavelength bands, respectively. Additionally, an SiN microring was also fabricated as presented in Figure 4a, with a 60- μm radius and a cross-section of $1\ \mu\text{m} \times 1.2\ \mu\text{m}$. This microring exhibited the typical intrinsic quality factors of 3.27×10^6 (at ~ 1550 nm) and 1.14×10^6 (at ~ 775 nm) for TM_0 modes (Figure 4c), corresponding to losses of 0.12 dB/cm and 0.33 dB/cm, which are consistent with the estimates of spiral waveguides.

Wave division multiplexing (WDM) is a key component in integrated optics. In our 3D PICs, the SiN WDM functions to combine and separate VI and IR light branches. As shown in Figure 4d, the SiN WDM comprises two closed parallel taper waveguides with a 600-nm

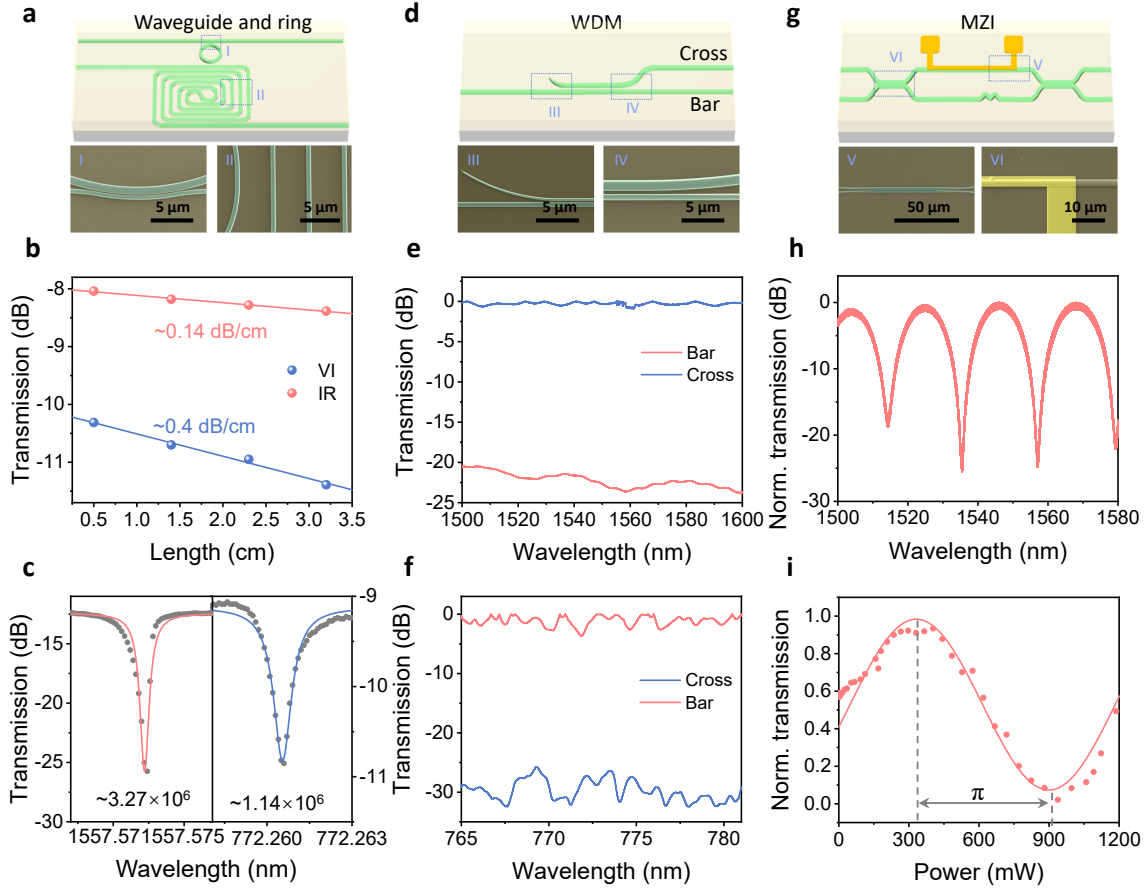


Figure 4: **Optical components of SiN PICs.** **a**, Schematic of SiN microring and spiral waveguide on SiO₂/sapphire. False-color SEM images of ring (I) and waveguide (II). **b**, Measured transmission intensities of SiN spiral waveguides with different lengths for IR and VI optical bands, respectively. **c**, Optical SiN micro-ring resonances with intrinsic quality factors of 3.27×10^6 and 1.14×10^6 for IR and VI TM₀ modes, respectively. **d**, Schematic of WDM and its zoom-in area (False-color SEM images (III) and (IV)). **e** and **f**, WDM transmission spectra of bar (blue) and cross (red) ports in IR and VI optical bands. **g**, Schematic of Mach-Zehnder interferometer (MZI) with thermal phase shifter on its one arm. False-color SEM images of MMI (V) and electrode (VI). **h**, Normalized transmission spectrum of MZI. **i**, Normalized transmission intensities of MZI tuned by thermal power with input wavelength at 1550 nm.

coupling gap and 1-mm coupling length. The device is optimized for optical TM_0 modes in both VI and IR bands, and the design details can be found in Supplementary Section V. Figure 4e is the calibrated WDM transmission spectrum in IR band. The IR light almost entirely couples into the cross port, while only smaller part (< -20 dB) passes through the bar port. Meanwhile, the insertion loss is only about 0.3 dB. Conversely, for the VI band, the bar port has near unitary transmission with minimal transmission of the cross port (< -25 dB), and the corresponding insertion loss is 1.1 dB.

Mach-Zehnder Interferometer (MZI) is a typical component used for controlling photon routing in PICs. To demonstrate this functionality in our 3D PICs, a SiN unbalanced MZI was fabricated with a specific design as depicted in Figure 4g. This MZI comprises two 50/50 multimode interference (MMI) couplers, and a phase shifter is placed on one arm. Due to symmetrical material structure, SiN hasn't an electro-optic coefficient. So, we use a heater as the phase shifter to tune the phase of optical modes via thermal-optic effect. SiN has a thermos-optic coefficient of $4.7 \times 10^{-5}/K$, smaller than that of Si ($1.84 \times 10^{-4}/K$). Numerical simulations were conducted to optimize the MMI structure parameters (Supplementary Section V). The IR transmission spectrum of unbalanced MZI is shown as Figure 4h, exhibiting a typical sinusoidal oscillation with an extinction ratio over 25 dB. Furthermore, we fixed the input optical wavelength at 1550 nm and controlled light output route and output power by fine-tuning MZI phase via the heater. Figure 4i shows the normalized output power at one MZI port, depending on heater's driving power. A π phase shift was achieved with about 600-mW power.

Optical link across AlN and SiN layers

Besides high-performance devices, reliable optical interconnects between stacked photonic layers are crucial for 3D PICs. Here, we proposed an adiabatic taper coupler to link SiN and AlN PIC layers as illustrated in Figure 5a. The coupler was designed with a 100-nm coupling gap, 100-nm tip width (W_e), 1.2- μ m waveguide width (W_s) and a coupling length

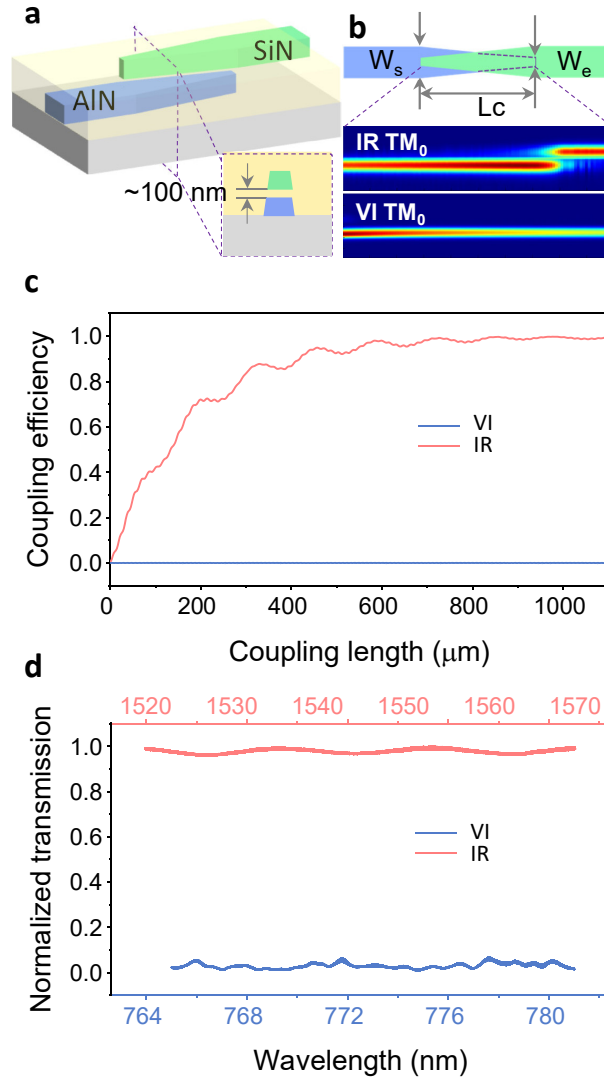


Figure 5: **Optical link between AlN and SiN PICs.** **a**, Schematic vertical coupler consists of AlN and SiN taper waveguides separated by a gap in vertical direction. **b**, Simulated mode profile distribution along directional coupler for IR and VI TM_0 modes. **c**, Simulated coupling efficiency from AlN to SiN as a function of the coupler length (L_c). **d**, Measured transmission spectrum of the coupler.

of L_c (Figure 5b). Numerical simulation was conducted to optimize L_c for maximizing the coupling efficiency of coupler. IR TM_0 mode of 1550 nm and VI TM_0 mode of 775 nm were selected as the operating optical modes based on our previous components of 3D PICs. The dependence of simulated coupling efficiency on coupling length L_c is illustrated as Figure 5c. For IR mode, the coupling efficiency increases with L_c and saturates near-unity at $L_c > 1000 \mu\text{m}$. While the VI mode has weak coupling between AlN and SiN taper waveguides, forbidding efficient optical crossing. Mode profile distributions within coupler waveguides for two optical modes are shown as in Figure 5b. Calibrated optical transmission spectra of coupler device for IR and VI wavelength bands are plotted in Figure 5d, presenting near-unity and near-zero coupling efficiencies for IR and VI modes, respectively. To achieve efficient vertical coupling for shorter wavelength bands, further optimizing coupler structures is necessary. Additionally, alternative methods such as vertical MMIs,⁷⁵ intermediate directional couplers,⁷⁶ and grating couplers,⁷⁷ offer viable solutions for realizing efficient broadband coupling.

Discussion

AlN, SiN, and Al_2O_3 have ultra-wideband optical transparency from ultraviolet to infrared, far beyond that of silicon.^{29,56,65,69,74} This positions them as ideal candidates for emerging applications of PICs working at short wavelengths.²⁰ Leveraging these three materials, we have developed 3D PICs via heterogeneous integration and demonstrated efficient SHG and SPDC, and low-loss and tunable optical components. Moreover, optical linking across vertical stacking layers was explored. We also assessed the ultra-low crossing loss between adjacent phonics layers by numerical simulation (Supplementary Section VI). Although the 3D PICs demonstrated promising performance of both optical non-linearity and linearity, there still remains significant room for improvement. First, the device fabrication processes need to be optimized to further minimize optical losses. For example, SiN PICs have al-

ready demonstrated optical losses as low as 1 dB/m and 0.1 dB/m at VI and IR wavelength bands,^{45,46,53,54} respectively, much better than our current results. Second, the structures of 3D PICs should be further optimized to achieve broadband optical vertical coupling. This may involve replacing the SiO₂ cladding material with Al₂O₃, reducing the thickness of AlN and SiN waveguide, and exploring other coupling structures such as vertical multimode interferometers and grating couplers.^{14,23,26,30} Finally, other optical components working at ultraviolet to visible bands remain to be unexplored.

Conclusion

In conclusion, we have developed a 3D PIC platform based on the vertical heterogeneous integration of AlN and SiN layers, enabling broadband operation across wavelengths from ultraviolet to infrared. The platform's efficient optical nonlinearity was validated through SHG and SPDC experiments performed in an AlN microring. Furthermore, we fabricated high-performance SiN optical components, such as low-loss microrings and waveguides, WDM devices, and tunable MZIs, demonstrating their immense potential for applications in 3D PICs. Optical interlayer transitions between AlN and SiN PICs were achieved via evanescent-field coupling between closely spaced waveguides. The scalability and integration density of our 3D PICs can be further enhanced by vertically stacking additional SiN waveguide layers. Additionally, thin III-nitride films, capable of photon generation and detection across ultraviolet to visible wavelengths,⁷⁸ can be directly integrated onto the PICs, thereby enabling the incorporation of numerous off-chip optical devices into a single chip. The integration of III-nitride-based ICs also offers a pathway to co-developing a 3D electronic-photonic integrated circuit ecosystem,^{15,79} potentially unlocking new possibilities for both classical and quantum information processing.

Methods

Device fabrication process can be found in the main text. Device measurements are detailedly described in supplementary materials.

Acknowledgement

LZ, YG, JY, JW and JL acknowledge the support from National Natural Science Foundation of China (62135013, 62274163, 62250071, 62234001); Beijing Nova Program 20230484466; Youth Innovation Promotion Association CAS 2022000028 and 2023123.

Author contributions

The experiments were conceived by LZ. The device was designed and fabricated by LZ. Measurements were performed by LZ. Analysis of the results was conducted by LZ. YG, JY, JW and JL support this work. All authors contribute to the preparation of manuscript.

Competing interests

The Authors declare no Competing Financial or Non-Financial Interests

Data availability

The data that support the findings of this study are available from the corresponding author upon reasonable request

Supporting Information Available

Vertical coupling design of AlN microring, theory of SHG and SPDC in microcavity, measurement of SHG and SPDC, design of SiN WDM and MMI, loss evaluation of vertical waveguide crossings

References

- (1) Chovan, J.; Uherek, F. Photonic integrated circuits for communication systems. *Radio-engineering* **2018**, *27*, 357–363.
- (2) Shen, Y.; Harris, N. C.; Skirlo, S.; Prabhu, M.; Baehr-Jones, T.; Hochberg, M.; Sun, X.; Zhao, S.; Larochelle, H.; Englund, D.; others Deep learning with coherent nanophotonic circuits. *Nature photonics* **2017**, *11*, 441–446.
- (3) Bogaerts, W.; Pérez, D.; Capmany, J.; Miller, D. A.; Poon, J.; Englund, D.; Morichetti, F.; Melloni, A. Programmable photonic circuits. *Nature* **2020**, *586*, 207–216.
- (4) Najafi, F.; Mower, J.; Harris, N. C.; Bellei, F.; Dane, A.; Lee, C.; Hu, X.; Kharel, P.; Marsili, F.; Assefa, S.; others On-chip detection of non-classical light by scalable integration of single-photon detectors. *Nature communications* **2015**, *6*, 5873.
- (5) Goossens, S.; Navickaite, G.; Monasterio, C.; Gupta, S.; Piqueras, J. J.; Pérez, R.; Burwell, G.; Nikitskiy, I.; Lasanta, T.; Galán, T.; others Broadband image sensor array based on graphene–CMOS integration. *Nature Photonics* **2017**, *11*, 366–371.
- (6) Xu, Z.; Zhou, T.; Ma, M.; Deng, C.; Dai, Q.; Fang, L. Large-scale photonic chiplet Taichi empowers 160-TOPS/W artificial general intelligence. *Science* **2024**, *384*, 202–209.

- (7) Bao, J.; Fu, Z.; Pramanik, T.; Mao, J.; Chi, Y.; Cao, Y.; Zhai, C.; Mao, Y.; Dai, T.; Chen, X.; others Very-large-scale integrated quantum graph photonics. *Nature Photonics* **2023**, *17*, 573–581.
- (8) Zhang, X.; Kwon, K.; Henriksson, J.; Luo, J.; Wu, M. C. A large-scale microelectromechanical-systems-based silicon photonics LiDAR. *Nature* **2022**, *603*, 253–258.
- (9) Brückerhoff-Plückelmann, F.; Bente, I.; Wendland, D.; Feldmann, J.; Wright, C. D.; Bhaskaran, H.; Pernice, W. A large scale photonic matrix processor enabled by charge accumulation. *Nanophotonics* **2023**, *12*, 819–825.
- (10) Liu, Y.; Shainline, J. M.; Zeng, X.; Popović, M. A. Ultra-low-loss CMOS-compatible waveguide crossing arrays based on multimode Bloch waves and imaginary coupling. *Optics letters* **2014**, *39*, 335–338.
- (11) Reif, R.; Fan, A.; Chen, K.-N.; Das, S. Fabrication technologies for three-dimensional integrated circuits. Proceedings International Symposium on Quality Electronic Design. 2002; pp 33–37.
- (12) Topol, A. W.; La Tulipe, D.; Shi, L.; Frank, D. J.; Bernstein, K.; Steen, S. E.; Kumar, A.; Singco, G. U.; Young, A. M.; Guarini, K. W.; others Three-dimensional integrated circuits. *IBM Journal of Research and Development* **2006**, *50*, 491–506.
- (13) Biberman, A.; Sherwood-Droz, N.; Zhu, X.; Preston, K.; Hendry, G.; Levy, J. S.; Chan, J.; Wang, H.; Lipson, M.; Bergman, K. Photonic network-on-chip architecture using 3D integration. Optoelectronic Integrated Circuits XIII. 2011; pp 130–133.
- (14) Shang, K.; Pathak, S.; Guan, B.; Liu, G.; Yoo, S. Low-loss compact multilayer silicon nitride platform for 3D photonic integrated circuits. *Optics Express* **2015**, *23*, 21334–21342.

- (15) Zhang, Y.; Samanta, A.; Shang, K.; Yoo, S. B. Scalable 3D silicon photonic electronic integrated circuits and their applications. *IEEE Journal of Selected Topics in Quantum Electronics* **2020**, *26*, 1–10.
- (16) Kim, T.; Bhargava, P.; Poulton, C. V.; Notaros, J.; Yaacobi, A.; Timurdogan, E.; Baiocco, C.; Fahrenkopf, N.; Kruger, S.; Ngai, T.; others A single-chip optical phased array in a wafer-scale silicon photonics/CMOS 3D-integration platform. *IEEE Journal of solid-state circuits* **2019**, *54*, 3061–3074.
- (17) Chang, P.-H.; Samanta, A.; Yan, P.; Fu, M.; Zhang, Y.; On, M. B.; Kumar, A.; Kang, H.; Yi, I.-M.; Annabattuni, D.; others A 3D integrated energy-efficient transceiver realized by direct bond interconnect of co-designed 12 nm finfet and silicon photonic integrated circuits. *Journal of Lightwave Technology* **2023**, *41*, 6741–6755.
- (18) Suzuki, K.; Konoike, R.; Yokoyama, N.; Seki, M.; Ohtsuka, M.; Saitoh, S.; Suda, S.; Matsuura, H.; Yamada, K.; Namiki, S.; others Nonduplicate polarization-diversity 32×32 silicon photonics switch based on a SiN/Si double-layer platform. *Journal of Lightwave Technology* **2020**, *38*, 226–232.
- (19) Contu, P.; Stagarescu, C.; Behfar, A.; Klamkin, J. 3D integrated silicon photonic external cavity laser (SPECL). 2014 IEEE Photonics Conference. 2014; pp 258–259.
- (20) Lu, X.; Chang, L.; Tran, M. A.; Komljenovic, T.; Bowers, J. E.; Srinivasan, K. Emerging integrated laser technologies in the visible and short near-infrared regimes. *Nature Photonics* **2024**, 1–14.
- (21) Guo, X.; Ji, X.; Yao, B.; Tan, T.; Chu, A.; Westreich, O.; Dutt, A.; Wong, C.; Su, Y. Ultra-wideband integrated photonic devices on silicon platform: from visible to mid-IR. *Nanophotonics* **2023**, *12*, 167–196.
- (22) Sorace-Agaskar, C.; Kharas, D.; Yegnanarayanan, S.; Maxson, R. T.; West, G. N.; Loh, W.; Bramhavar, S.; Ram, R. J.; Chiaverini, J.; Sage, J.; others Versatile silicon

- nitride and alumina integrated photonic platforms for the ultraviolet to short-wave infrared. *IEEE Journal of Selected Topics in Quantum Electronics* **2019**, *25*, 1–15.
- (23) Lin, Y.; Mak, J. C.; Chen, H.; Mu, X.; Stalmashonak, A.; Jung, Y.; Luo, X.; Lo, P. G.-Q.; Sacher, W. D.; Poon, J. K. Low-loss broadband bi-layer edge couplers for visible light. *Optics Express* **2021**, *29*, 34565–34576.
- (24) West, G. N.; Loh, W.; Kharas, D.; Sorace-Agaskar, C.; Mehta, K. K.; Sage, J.; Chiverini, J.; Ram, R. J. Low-loss integrated photonics for the blue and ultraviolet regime. *Apl Photonics* **2019**, *4*, 026101.
- (25) Mu, J.; Dijkstra, M.; Yong, Y.-S.; de Goede, M.; Chang, L.; García-Blanco, S. M. Monolithic Integration of Al₂O₃ and Si₃N₄ Toward Double-Layer Active–Passive Platform. *IEEE Journal of Selected Topics in Quantum Electronics* **2019**, *25*, 1–11.
- (26) Mu, J.; Dijkstra, M.; García-Blanco, S. M. Resonant coupling for active–passive monolithic integration of Al₂O₃ and Si₃N₄. *IEEE Photonics Technology Letters* **2019**, *31*, 771–774.
- (27) Dong, M.; Heim, D.; Witte, A.; Clark, G.; Leenheer, A. J.; Dominguez, D.; Zimmermann, M.; Wen, Y. H.; Gilbert, G.; Englund, D.; others Piezo-optomechanical cantilever modulators for VLSI visible photonics. *APL Photonics* **2022**, *7*, 051304.
- (28) Zhu, S.; Lo, G.-Q. Vertically stacked multilayer photonics on bulk silicon toward three-dimensional integration. *Journal of Lightwave Technology* **2015**, *34*, 386–392.
- (29) Sorace-Agaskar, C.; Bramhavar, S.; Kharas, D.; Loh, W.; Juodawlkis, P. W.; Chiverini, J.; Sage, J. M. Multi-layer integrated photonics from the ultraviolet to the infrared. *Frontiers in Biological Detection: From Nanosensors to Systems X*. 2018; pp 36–45.

- (30) Lin, Y.; Yong, Z.; Luo, X.; Azadeh, S. S.; Mikkelsen, J. C.; Sharma, A.; Chen, H.; Mak, J. C.; Lo, P. G.-Q.; Sacher, W. D.; others Monolithically integrated, broadband, high-efficiency silicon nitride-on-silicon waveguide photodetectors in a visible-light integrated photonics platform. *Nature Communications* **2022**, *13*, 6362.
- (31) Dong, M.; Clark, G.; Leenheer, A. J.; Zimmermann, M.; Dominguez, D.; Menssen, A. J.; Heim, D.; Gilbert, G.; Englund, D.; Eichenfield, M. High-speed programmable photonic circuits in a cryogenically compatible, visible–near-infrared 200 mm CMOS architecture. *Nature Photonics* **2022**, *16*, 59–65.
- (32) Ludwig, M.; Ayhan, F.; Schmidt, T. M.; Wildi, T.; Voumard, T.; Blum, R.; Ye, Z.; Lei, F.; Wildi, F.; Pepe, F.; others Ultraviolet astronomical spectrograph calibration with laser frequency combs from nanophotonic lithium niobate waveguides. *Nature Communications* **2024**, *15*, 7614.
- (33) Biberman, A.; Shaw, M. J.; Timurdogan, E.; Wright, J. B.; Watts, M. R. Ultralow-loss silicon ring resonators. *Optics letters* **2012**, *37*, 4236–4238.
- (34) Tran, M. A.; Huang, D.; Komljenovic, T.; Peters, J.; Malik, A.; Bowers, J. E. Ultra-low-loss silicon waveguides for heterogeneously integrated silicon/III-V photonics. *Applied Sciences* **2018**, *8*, 1139.
- (35) Wilmart, Q.; Brisson, S.; Hartmann, J.-M.; Myko, A.; Ribaud, K.; Petit-Etienne, C.; Youssef, L.; Fowler, D.; Charbonnier, B.; Sciancalepore, C.; others A complete Si photonics platform embedding ultra-low loss waveguides for O-and C-band. *Journal of Lightwave Technology* **2020**, *39*, 532–538.
- (36) Ciminelli, C.; Dell’Olio, F.; Armenise, M. N.; Soares, F. M.; Passenberg, W. High performance InP ring resonator for new generation monolithically integrated optical gyroscopes. *Optics Express* **2013**, *21*, 556–564.

- (37) Chang, L.; Xie, W.; Shu, H.; Yang, Q.-F.; Shen, B.; Boes, A.; Peters, J. D.; Jin, W.; Xiang, C.; Liu, S.; others Ultra-efficient frequency comb generation in AlGaAs-on-insulator microresonators. *Nature communications* **2020**, *11*, 1331.
- (38) Chang, L.; Boes, A.; Pintus, P.; Xie, W.; Peters, J. D.; Kennedy, M.; Jin, W.; Guo, X.-W.; Yu, S.-P.; Papp, S. B.; others Low loss (Al) GaAs on an insulator waveguide platform. *Optics Letters* **2019**, *44*, 4075–4078.
- (39) Apiratikul, P.; Wathen, J. J.; Porkolab, G. A.; Wang, B.; He, L.; Murphy, T. E.; Richardson, C. J. Enhanced continuous-wave four-wave mixing efficiency in nonlinear AlGaAs waveguides. *Optics express* **2014**, *22*, 26814–26824.
- (40) Sugimoto, Y.; Tanaka, Y.; Ikeda, N.; Nakamura, Y.; Asakawa, K.; Inoue, K. Low propagation loss of 0.76 dB/mm in GaAs-based single-line-defect two-dimensional photonic crystal slab waveguides up to 1 cm in length. *Optics Express* **2004**, *12*, 1090–1096.
- (41) Li, Z.; Wang, R. N.; Lihachev, G.; Zhang, J.; Tan, Z.; Churaev, M.; Kuznetsov, N.; Siddharth, A.; Bereyhi, M. J.; Riemensberger, J.; others High density lithium niobate photonic integrated circuits. *Nature Communications* **2023**, *14*, 4856.
- (42) Zhang, M.; Wang, C.; Cheng, R.; Shams-Ansari, A.; Lončar, M. Monolithic ultra-high-Q lithium niobate microring resonator. *Optica* **2017**, *4*, 1536–1537.
- (43) Gao, R.; Yao, N.; Guan, J.; Deng, L.; Lin, J.; Wang, M.; Qiao, L.; Fang, W.; Cheng, Y. Lithium niobate microring with ultra-high Q factor above 10⁸. *Chinese Optics Letters* **2022**, *20*, 011902.
- (44) Hwang, E.; Harper, N.; Sekine, R.; Ledezma, L.; Marandi, A.; Cushing, S. Tunable and efficient ultraviolet generation with periodically poled lithium niobate. *Optics Letters* **2023**, *48*, 3917–3920.

- (45) Puckett, M. W.; Liu, K.; Chauhan, N.; Zhao, Q.; Jin, N.; Cheng, H.; Wu, J.; Behunin, R. O.; Rakich, P. T.; Nelson, K. D.; others 422 Million intrinsic quality factor planar integrated all-waveguide resonator with sub-MHz linewidth. *Nature communications* **2021**, *12*, 934.
- (46) Yong, Z.; Chen, H.; Luo, X.; Govdeli, A.; Chua, H.; Azadeh, S. S.; Stalmashonak, A.; Lo, G.-Q.; Poon, J. K.; Sacher, W. D. Power-efficient silicon nitride thermo-optic phase shifters for visible light. *Optics express* **2022**, *30*, 7225–7237.
- (47) Subramanian, A.; Neutens, P.; Dhakal, A.; Jansen, R.; Claes, T.; Rottenberg, X.; Peyskens, F.; Selvaraja, S.; Helin, P.; Du Bois, B.; others Low-loss singlemode PECVD silicon nitride photonic wire waveguides for 532–900 nm wavelength window fabricated within a CMOS pilot line. *IEEE Photonics Journal* **2013**, *5*, 2202809–2202809.
- (48) Smith, J. A.; Francis, H.; Navickaite, G.; Strain, M. J. SiN foundry platform for high performance visible light integrated photonics. *Optical Materials Express* **2023**, *13*, 458–468.
- (49) Chauhan, N.; Wang, J.; Bose, D.; Moreira, R.; Blumenthal, D. J. Ultra-low loss 698 nm and 450 nm silicon nitride visible wavelength waveguides for strontium atomic clock applications. CLEO: Science and Innovations. 2020; pp STh1J–2.
- (50) Corato-Zanarella, M.; Ji, X.; Mohanty, A.; Lipson, M. Absorption and scattering limits of silicon nitride integrated photonics in the visible spectrum. *Optics Express* **2024**, *32*, 5718–5728.
- (51) Morin, T. J.; Chang, L.; Jin, W.; Li, C.; Guo, J.; Park, H.; Tran, M. A.; Komljenovic, T.; Bowers, J. E. CMOS-foundry-based blue and violet photonics. *Optica* **2021**, *8*, 755–756.
- (52) Buzaverov, K. A.; Baburin, A. S.; Sergeev, E. V.; Avdeev, S. S.; Lotkov, E. S.; Andronik, M.; Stukalova, V. E.; Baklykov, D. A.; Dyakonov, I. V.; Skryabin, N. N.; others

- Low-loss silicon nitride photonic ICs for near-infrared wavelength bandwidth. *Optics Express* **2023**, *31*, 16227–16242.
- (53) Ji, X.; Barbosa, F. A.; Roberts, S. P.; Dutt, A.; Cardenas, J.; Okawachi, Y.; Bryant, A.; Gaeta, A. L.; Lipson, M. Ultra-low-loss on-chip resonators with sub-milliwatt parametric oscillation threshold. *Optica* **2017**, *4*, 619–624.
- (54) Chanana, A.; Larocque, H.; Moreira, R.; Carolan, J.; Guha, B.; Melo, E. G.; Anant, V.; Song, J.; Englund, D.; Blumenthal, D. J.; others Ultra-low loss quantum photonic circuits integrated with single quantum emitters. *Nature Communications* **2022**, *13*, 7693.
- (55) Liu, X.; Bruch, A. W.; Gong, Z.; Lu, J.; Surya, J. B.; Zhang, L.; Wang, J.; Yan, J.; Tang, H. X. Ultra-high-Q UV microring resonators based on a single-crystalline AlN platform. *Optica* **2018**, *5*, 1279–1282.
- (56) Lu, T.-J.; Fanto, M.; Choi, H.; Thomas, P.; Steidle, J.; Mouradian, S.; Kong, W.; Zhu, D.; Moon, H.; Berggren, K.; others Aluminum nitride integrated photonics platform for the ultraviolet to visible spectrum. *Optics express* **2018**, *26*, 11147–11160.
- (57) Liu, X.; Gong, Z.; Bruch, A. W.; Surya, J. B.; Lu, J.; Tang, H. X. Aluminum nitride nanophotonics for beyond-octave soliton microcomb generation and self-referencing. *Nature communications* **2021**, *12*, 5428.
- (58) Bruch, A. W.; Liu, X.; Guo, X.; Surya, J. B.; Gong, Z.; Zhang, L.; Wang, J.; Yan, J.; Tang, H. X. 17000%/W second-harmonic conversion efficiency in single-crystalline aluminum nitride microresonators. *Applied Physics Letters* **2018**, *113*, 131102.
- (59) Sun, Y.; Shin, W.; Laleyan, D. A.; Wang, P.; Pandey, A.; Liu, X.; Wu, Y.; Soltani, M.; Mi, Z. Ultrahigh Q microring resonators using a single-crystal aluminum-nitride-on-sapphire platform. *Optics letters* **2019**, *44*, 5679–5682.

- (60) Liu, K.; Yao, S.; Ding, Y.; Wang, Z.; Guo, Y.; Yan, J.; Wang, J.; Yang, C.; Bao, C. Fundamental linewidth of an AlN microcavity Raman laser. *Optics Letters* **2022**, *47*, 4295–4298.
- (61) McKay, E.; Pruiti, N. G.; May, S.; Sorel, M. High-confinement alumina waveguides with sub-dB/cm propagation losses at 450 nm. *Scientific Reports* **2023**, *13*, 19917.
- (62) Demirtaş, M.; Odacı, C.; Perkgöz, N. K.; Sevik, C.; Ay, F. Low loss atomic layer deposited Al₂O₃ waveguides for applications in on-chip optical amplifiers. *IEEE Journal of Selected Topics in Quantum Electronics* **2018**, *24*, 1–8.
- (63) De Goede, M.; Dijkstra, M.; Obregón, R.; Ramón-Azcón, J.; Martínez, E.; Padilla, L.; Mitjans, F.; Garcia-Blanco, S. M. Al₂O₃ microring resonators for the detection of a cancer biomarker in undiluted urine. *Optics express* **2019**, *27*, 18508–18521.
- (64) Bradley, J.; Ay, F.; Wörhoff, K.; Pollnau, M. Fabrication of low-loss channel waveguides in Al₂O₃ and Y₂O₃ layers by inductively coupled plasma reactive ion etching. *Applied Physics B* **2007**, *89*, 311–318.
- (65) Aslan, M. M.; Webster, N. A.; Byard, C. L.; Pereira, M. B.; Hayes, C. M.; Wiederkehr, R. S.; Mendes, S. B. Low-loss optical waveguides for the near ultra-violet and visible spectral regions with Al₂O₃ thin films from atomic layer deposition. *Thin Solid Films* **2010**, *518*, 4935–4940.
- (66) Ranno, L.; Sia, J. X. B.; Dao, K. P.; Hu, J. Multi-material heterogeneous integration on a 3-D photonic-CMOS platform. *Optical Materials Express* **2023**, *13*, 2711–2725.
- (67) Franken, C.; Hendriks, W.; Winkler, L.; Dijkstra, M.; do Nascimento Jr, A.; van Rees, A.; Mardani, M.; Dekker, R.; van Kerkhof, J.; van der Slot, P.; others Hybrid integrated near UV lasers using the deep-UV Al₂O₃ platform. *arXiv preprint* **2023**, arXiv:2302.11492.

- (68) Op de Beeck, C.; Mayor, F. M.; Cuyvers, S.; Poelman, S.; Herrmann, J. F.; Atalar, O.; McKenna, T. P.; Haq, B.; Jiang, W.; Witmer, J. D.; others III/V-on-lithium niobate amplifiers and lasers. *Optica* **2021**, *8*, 1288–1289.
- (69) Li, N.; Ho, C. P.; Zhu, S.; Fu, Y. H.; Zhu, Y.; Lee, L. Y. T. Aluminium nitride integrated photonics: a review. *Nanophotonics* **2021**, *10*, 2347–2387.
- (70) Dobrovinskaya, E. R.; Lytvynov, L. A.; Pishchik, V. *Sapphire: material, manufacturing, applications*; Springer Science & Business Media, 2009.
- (71) Zhang, L.; Cui, C.; Yan, J.; Guo, Y.; Wang, J.; Fan, L. On-chip parallel processing of quantum frequency comb. *npj Quantum Information* **2023**, *9*, 57.
- (72) Bruch, A. W.; Liu, X.; Gong, Z.; Surya, J. B.; Li, M.; Zou, C.-L.; Tang, H. X. Pockels soliton microcomb. *Nature Photonics* **2021**, *15*, 21–27.
- (73) Chen, H.; Zhou, J.; Li, D.; Chen, D.; Vinod, A. K.; Fu, H.; Huang, X.; Yang, T.-H.; Montes, J. A.; Fu, K.; others Supercontinuum generation in high order waveguide mode with near-visible pumping using aluminum nitride waveguides. *ACS Photonics* **2021**, *8*, 1344–1352.
- (74) Liu, X.; Bruch, A. W.; Lu, J.; Gong, Z.; Surya, J. B.; Zhang, L.; Wang, J.; Yan, J.; Tang, H. X. Beyond 100 THz-spanning ultraviolet frequency combs in a non-centrosymmetric crystalline waveguide. *Nature communications* **2019**, *10*, 2971.
- (75) Brooks, C. J.; Knights, A. P.; Jessop, P. E. Vertically-integrated multimode interferometer coupler for 3D photonic circuits in SOI. *Optics Express* **2011**, *19*, 2916–2921.
- (76) Takei, R.; Maegami, Y.; Omoda, E.; Sakakibara, Y.; Mori, M.; Kamei, T. Low-loss and low wavelength-dependence vertical interlayer transition for 3D silicon photonics. *Optics express* **2015**, *23*, 18602–18610.

- (77) Sodagar, M.; Pourabolghasem, R.; Eftekhar, A. A.; Adibi, A. High-efficiency and wide-band interlayer grating couplers in multilayer Si/SiO₂/SiN platform for 3D integration of optical functionalities. *Optics express* **2014**, *22*, 16767–16777.
- (78) Razeghi, M. III-nitride optoelectronic devices: from ultraviolet toward terahertz. *IEEE Photonics Journal* **2011**, *3*, 263–267.
- (79) Xiang, C.; Bowers, J. E. Building 3D integrated circuits with electronics and photonics. *Nature Electronics* **2024**, *7*, 422–424.